Improving the impervious surface estimation with combined use of optical and SAR remote sensing images

CrossMark

Yuanzhi Zhang [a,b], Hongsheng Zhang [a,*], Hui Lin [a]

[a] Institute of Space and Earth Information Science & Shenzhen Research Institute, The Chinese University of Hong Kong (CUHK), Shatin, New Territories, Hong Kong
[b] National Astronomical Observatories, Chinese Academy of Sciences, Beijing 100012, China

ARTICLE INFO

ABSTRACT

Accurate mapping of urban impervious surfaces is important but challenging due to the diversity of urban land covers. This study presents an effort to synergistically combine optical and SAR data to improve the mapping of impervious surfaces. Three pairs of optical and SAR images, Landsat ETM + and ENVISAT ASAR, SPOT-5 and ENVISAR ASAR, and SPOT-5 and TerraSAR-X, were selected in three study areas to validate the effectiveness of the methods in this study. The potential of Random Forest (RF) was evaluated with parameter optimization for combining the optical and SAR images. Experiment results demonstrate some interesting findings. Firstly, the built-in out-of-bag (OOB) error is insufficient for accuracy assessment, and an assessment with additional reference data is required for combining optical and SAR images using RF. Secondly, the optimal number of variables (m) for splitting the decision tree nodes in RF should be some different from the principles reported previously, and an empirical relationship was given for determining the parameter m. Thirdly, the optimal number of decision trees (T) in RF is not sensitive to the resolutions and sensor types of optical and SAR images, and the optimal T in this study is 20. Fourthly, the combined use of optical and SAR images by using RF is effective to improve the land cover classification and impervious surface estimation, by reducing the confusions between bright impervious surface and bare soil and dark impervious surface and bare soil, as well as shaded area and water surface. Even though the easily-confused land classes tend to be different in different resolutions of images, the effectiveness of combining optical and SAR images is consistent. This improvement is more significant when combing lower resolution optical and SAR images. The conclusions of this study could serve as an important reference for further applications of optical and SAR images, and as a potential reference for the applications of RF to the fusion of other multi-source remote sensing data.

© 2013 Elsevier Inc. All rights reserved.

1. Introduction

Urban impervious surfaces, such as transport related land (e.g., roads, streets, and parking lots) and building roof tops (commercial, residential, and industrial areas), have been widely recognized as important indicator for urban environments (Arnold & Gibbons, 1996; Hurd & Civco, 2004; Lu & Weng, 2006; Weng, 2001; Weng, Lu, & Liang, 2006; Yuan & Bauer, 2007). Remote sensing has become the major technique to estimate impervious surfaces due to its low cost and convenience for the impervious surface mapping from local to global scales. Numerous methods have been proposed to estimate impervious surfaces from remotely sensed images, including sub-pixel approaches (e.g., the spectral mixture analysis method (Wu & Murray, 2003; Wu, 2004), the classification and regression tree model (Yang, Xian, Klaver, & Deal, 2003), the artificial neural network (Weng & Hu, 2008), and the support vector machine (Sun, Guo, Li, Lu, & Du, 2011)) and per-pixel approaches such as conventional classification methods (Weng, 2012). Recently, a biophysical composition index (BCI) was proposed to extract urban impervious surfaces following

the VIS conceptual model (Deng & Wu, 2012). However, most of these approaches were proposed with optical remote sensing images, and accurate estimation of impervious surfaces remains challenging due to the diversity of urban land covers, leading to difficulties of separating different land covers with similar spectral signatures (Weng, 2012). For instance, dry soils or sands are reported to be confused with bright impervious surfaces due to their high reflectance, while water and shades tend to be confused with dark impervious surfaces.

The use of multi-satellite images is considered as one promising approach to improve the accuracy of impervious surfaces (Weng, 2012). SAR is able to provide useful information about urban areas as it is sensitive to the geometric characteristics of urban land surfaces (Calabresi, 1996; Henderson & Xia, 1997; Leinenkugel, Esch, & Kuenzer, 2011; Soergel, 2010; Tison, Nicolas, Tupin, & Maitre, 2004; Zhang, Zhang, & Lin, 2012), and thus SAR has been identified as an important source to help extract impervious surfaces with optical data (Jiang, Liao, Lin, & Yang, 2009; Weng, 2012; Yang, Jiang, Lin, & Liao, 2009). Fusion between optical and SAR data can be performed on three different levels: pixel-level, feature-level, and decision-level. Pixel-level fusion is reported inappropriate for SAR images because of speckle noises (Zhang, Yang, Zhao, Li, & Zhang, 2010). For feature-level

* Corresponding author. Tel.: +852 39434280; fax: +852 26037470.
E-mail address: zhangstream@gmail.com (H. Zhang).

fusion, several approaches have been proposed including layer-stacking and ensemble-learning methods (e.g., bagging, boosting, AdaBoost & Random Forest (Hall & Llinas, 1997; Rokach, 2010)). The ensemble-learning methods can be combined with different classifiers (e.g., ANN and SVM (Rokach, 2010)). For decision-level fusion, various weighting methods (e.g., majority voting, entropy weighting, and performance weighting) and the Dempster–Shafer theory have been applied. However, conventional classifiers with a layer-stacking technique are not appropriate in this case as optical reflectance and SAR backscattering data do not correlate (Zhang et al., 2010). Among these methods, the decision-tree (DT) method will be given more attention, while the Random Forest (RF) algorithm has been reported to perform excellently in the fusion of optical and SAR data (Waske & van der Linden, 2008). However, the potential and effectiveness of RF on the fusion between optical and SAR images needs to be explored, especially in terms of the estimation of urban impervious surfaces.

This study aims to evaluate the effectiveness of RF to synergistically combine the optical and SAR data in terms of impervious surface estimation. A combination of pixel level and feature level fusion method is adopted. Additionally, the Kappa coefficient based on confusion matrix and the OOB error built-in the RF are compared to assess the effectiveness of fusing optical and SAR images.

2. Study area and data sets

2.1. Study area

Three cities, Guangzhou, Shenzhen and Hong Kong, located in the Pearl River Delta (PRD) are selected as the study areas to evaluate the effectiveness of the proposed approach. The region is located on the Pearl River Estuary (PRE), known as the third largest metropolitan area in China, experiencing tremendously fast development during the past 30 years. The region has rapidly become urbanized, with a population of over 19 million in an area of over 21 thousand km^2 (Fan, Wang, & Wang, 2008). However, due to significant interactions between human population and environment, environmental issues quickly emerged causing a series of problems, including air and water pollution (Zhang et al., 2008). As key indicators of urban growth and related environmental problems, impervious surfaces and their distribution are being paid greater attention by the local government. Thus, the accurate estimation of urban impervious surfaces is of high significance for the environment studies of PRD.

2.2. Satellite data and coregistration

Three different combinations of optical and SAR satellite data sets are selected for the three cities (Fig. 1). For Guangzhou, a scene of Landsat ETM + image and a scene of ENVISAT Advanced Synthetic Aperture Radar (ASAR) Wide Swath Mode (WSM) image are employed. The ETM + images have one panchromatic band at 15 m resolution and 6 bands at 30 m resolution. In this study, only the 30-m data were used. The ETM + image was acquired on 31 December 2010. As there are stripes on the eastern and western edges of each scene because of the footprints (location and spatial extent) of each band due to the Scan Line Corrector (SLC) failure, a process should be applied to get rid of these stripes. For this reason, the study area is located in the middle of each scene where there are no stripes, and thus no stripe removal operation should be applied. We assume that the atmospheric condition is clear and homogeneous and the small part of clouds would not significantly impact the whole scene of image, and thus no atmospheric correction was performed (Wu & Murray, 2003). The ENVISAT ASAR WSM data were obtained on 23 September, 2010, on the descending direction with V/V polarization and a pixel size of 75 × 75 m.

For the Shenzhen City, a scene of SPOT-5 image and a scene of ENVISAT ASAR ASA_IMP_1P data are used. The SPOT-5 image is a precision 2A level data, and was obtained on 21 November 2008, with

a spatial resolution of 10 m. The ASAR data were obtained on 19 November 2008, on the ascending direction, Track-25 of ENVISAT, with V/V polarization. The spatial resolution of the ASAR IMP data is 12.5 m. Due to the speckle noises, Enhanced Lee filter is selected to filter the speckle noises in the ASAR data. Enhanced Lee filter is an improved version of Lee filter which was designed to better and preserve texture information, edges, linear features and point targets in SAR images (Lee, 1983). Enhanced Lee filter is an adaptive filter which was proved to be more suitable for preserving radiometric and textural information than other speckle filters (Lopes, Touzi, & Nezry, 1990; Xie, Pierce, & Ulaby, 2002).

For Hong Kong, a SPOT-5 and a SAR image from TerraSAR-X are employed. The SPOT-5 image is also a precision 2A level data, and was obtained on 21 November 2008, with a spatial resolution of 10 m. TerraSAR-X (TSX) is a German earth observation satellite launched on 15 June 2007 and is still on operation. TSX operates in the X band (9.6 GHz) and has three main imaging modes, SpotLight, StripMap and ScanSAR. The TSX image used in this study was obtained in the StripMap mode, on 16 November 2008, with a spatial resolution of 3 × 3 m, and the scene size is 30 km (width) × 50 km (length). The TSX image was geocoded with the NEST (Next ESA SAR Toolbox) 4C-1.1 software developed by ESA, under the coordinate system of WGS84 and UTM (Zone 50N). Moreover, geometric correction was also conducted by the Range-Doppler Terrain Correction in NEST with Digital Elevation Model (DEM) data. Additionally, due to the uncertainty of speckle noises in SAR images, Enhanced Lee filter is selected to filter the speckle noises.

After preprocessing all the satellite images, both optical images and SAR images were coregistered to the same geo-reference system of the Universal Transverse Mercator (UTM) projection (Zone 50N) and Datum World Geodetic System 84 (WGS84). Over 20 control points were manually selected for each pair of optical and SAR images, and the linear transformation approach is used to conduct the coregistration. The spatial resolutions of the final registered images are determined by the corresponding optical image which is clearer for human perception and easier for the manual selection of control points (Table 1). The Root Mean Square Error (RMSE) of the coregistration for each pair of optical and SAR images is less than half pixel.

3. Methods

3.1. Feature extraction

According to previous literatures, segmentation methods are superior over pixel by pixel methods as segmentation methods take the texture characteristics into account (Dell'Acqua & Gamba, 2003; Stasolla & Gamba, 2008). Texture is important for the interpretation of SAR data because the speckles in SAR data result in difficulties for the pixel by pixel approach. Therefore, in order to extract complementary information for urban impervious surfaces from optical and SAR images, texture feature extraction is necessary and important. In this paper, the popular gray level co-occurrence matrix (GLCM) approach (Haralick, Shanmuga, & Dinstein, 1973) is employed to analyze the texture features. For the application of GLCM, the size of image block and the texture measures with GLCM have been a major issue (Marceau, Howarth, Dubois, & Gratton, 1990). In terms of the classification of remote sensing images in urban areas, it is reported that a window size of 7 × 7 pixels is suitable with a test on the resolutions from 2.5 m × 2.5 m to 10 m × 10 m (Puissant, Hirsch, & Weber, 2005). Moreover, four texture measures, the homogeneity (HOM), dissimilarity (DISS), entropy (ENT), and the angular second moment (ASM), were identified as effective indicators for the texture description of different urban land cover types (Puissant et al., 2005). However, since the spatial resolution of the registered Landsat ETM + and ASAR image is 30 m, the window size for calculating GLCM should be smaller as terrains are smaller under coarser resolution. Thus, in this study, the window size is set as 7 × 7 pixels for Shenzhen and Hong
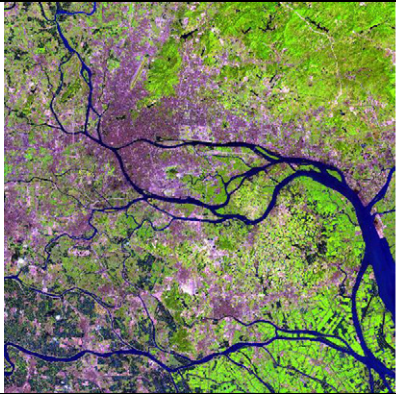
Study Areas	Optical Images	SAR Images
	Landsat ETM+	ENVISAT ASAR (WSM)
Guangzhou		
	SPOT-5	ENVISAT ASAR (IMP)
Shenzhen		
	SPOT-5	TerraSAR-X
Hong Kong		

Fig. 1. Comparison of ISA estimation with optimal parameter configurations.

Table 1
Coregistration design between optical and SAR images.

Study areas	Optical image (base image)		SAR image		Registered result
	Satellite sensor	Resolution (m)	Satellite sensor	Resolution (m)	Resolution (m)
Guangzhou	Landsat ETM +	30	ENVISAT ASAR (WSM)	75	75
Shenzhen	SPOT-5	10	ENVISAT ASAR (IMP)	12.5	10
Hong Kong	SPOT-5	10	TerraSAR-X	3	10

Table 2
Number of bands and features as the input into the RF algorithm.

Study area	Number of bands	Number of texture feature images	Total number of images input into RF
Guangzhou	7	28	35
Shenzhen	5	20	25
Hong Kong	5	20	25

Kong cases, and 3 × 3 for the Guangzhou case. Four texture measures, HOM, DISS, ENT, and ASM, are employed for all the three cases.

If we combine the SAR image as a band to the optical images, then we can calculate the total number of images (bands) which are the input of RF. Table 2 shows the number of band and number of texture features from both optical and SAR images, and the total number of images input into the RF algorithm. It shows that there are a total of 35 variables for the Guangzhou case, 25 variables for Shenzhen, and 25 variables for Hong Kong.

3.2. The Random Forest (RF) algorithm

The general strategy of RF was proposed by Breiman (2001), which is based on randomly re-sampling the input training data. RF has been applied in diverse remote sensing studies (Gislason, Benediktsson, & Sveinsson, 2006; Ham, Chen, Crawford, & Ghosh, 2005; Pal, 2003), and is proved to have a comparable performance to more complex methods like support vector machine which is much more time consuming (Guo, Chehata, & Boukir, 2010; Guo, Chehata, Mallet, & Boukir, 2011; Waske & van der Linden, 2008). Several advantages make RF suitable for remote sensing studies (Guo et al., 2011; Yu, Hyyppa, Vastaranta, Holopainen, & Viitala, 2011). Firstly, RF does not overfit when the number of trees increases (Breiman, 2001). Secondly, RF does not need any additional feature selection since a random selection of features is built in it (Yu et al., 2011). Thirdly, RF makes no distributional assumptions about the data sets and can handle situations where the training data set is small while the predicted data set is large (Cutler, Edwards, Beard, Cutler, & Hess, 2007).

The basic idea of RF is to grow multiple decision trees on the random subsets of the training data and related variables (Stumpf & Kerle, 2011). A brief description for this algorithm is as follows:

Input: N training samples, with M variables/features in each sample, and μ is the size of subset of training samples, $\mu < N$.
Output: a trained Random Forest with T decision trees:
1. Choose a training subset for a tree with replacement by T iterations in all training samples;
2. For each node, randomly choose m variables to determine the decision rules at that node. Calculate the best split based on these m variables in the training subset ($m < M$);
3. Return to step 1 until T iterations end.

Fig. 2 illustrates the basic flowchart of the RF algorithm. In the first step, to build a decision tree, about one third of training samples are left out by the random selection, and these samples are called out-of-bag samples (Yu et al., 2011). The out-of-bag (OOB) samples are used as the testing data for the grown decision tree. When building a decision tree, each tree node will be determined by m variables randomly selected from the M variables. After the training procedure, T decision trees are built as the Random Forest, which will be used as the classifier. To classify each new pixel, each decision tree will get a classification result as a vote to that class. Finally, the class with majority votes from all the decision trees will be assigned as the class of the pixel.

In this study, one training sample corresponds with the location of a pixel, with the M variables/features representing the feature information from both optical and SAR images. In particular, a training sample in this case can be expressed as a vector consisting of the following two components (two groups of features): 1) reflectance of each optical band and 2) texture features of the ASAR images. The first group is from optical images and the second is derived from SAR data. For the texture features of the ASAR image, the gray level co-occurrence matrix (GLCM) is applied to extract the texture features (Haralick et al., 1973).

3.3. Parameter configuration of Random Forest (RF)

The success of RF depends on the prediction accuracy of each decision tree and the correlation between different decision trees
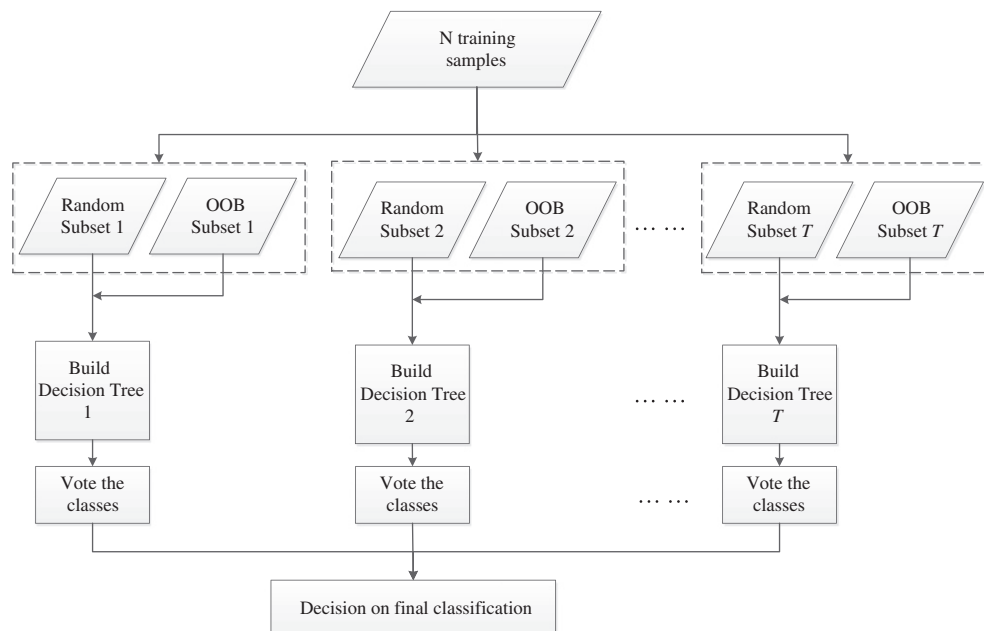

Fig. 2. Flowchart of the Random Forest (RF) algorithm.

(Breiman, 2001). In order to reduce correlation, two random selection procedures are employed (Yu et al., 2011): 1) a random selection of train samples in each of the T iterations to grow each decision tree and 2) a random selection of variables (or features) to select m variables to determine each node in a tree. Therefore, two parameters are significant for the success of RF in the fusion of optical and SAR images, the number of decision trees (T) and the number of features (m) at each node for spilling.

For the number of trees, it was reported that T can be any value defined by the user (Pal, 2003). For the number of features, previous studies suggested m to be the root of the total number of features (Gislason et al., 2006; Stumpf & Kerle, 2011). However, in previous applications of RF, there are often a number of features, while the number of features in this case for the impervious surface estimation is very limited. Thus, it is still not clear what the optimal number should be for the random selection of features. Therefore, in this paper, a quantitative analysis is designed to test the impacts of T and m on the performance of RF for the fusion of optical and SAR data for impervious surface estimation.

In addition, the splitting rule is also important for the selection of features. There are several selection approaches in literatures, e.g., the Quinlan's Information Gain Ratio (Quinlan, 1986), the *Gini* Index (Breiman, 1984), and the Mingers's G statistic (Mingers, 1989). However, the *Gini* Index is the most frequently used for RF as it measures the impurity of an attribute by searching the largest class and isolating it from the rest of the data (Breiman, 1984; Pal, 2003). In this study, the *Gini* Index is employed to measure the impurity for each node to find the best combination of features (variables). The following equation describes the *Gini* index of note t (Zambon, Lawrence, Bunn, & Powell, 2006):

$$Gini(t) = \sum_{i=1}^{L} p_i (1 - p_i) \tag{1}$$

where p_i denotes the relative frequency of each class in the training subset, and L is the total number of classes. p_i can be determined by dividing the total number of samples of the class i by the total number of samples in the subset.

3.4. Classification strategy and accuracy assessment

Mapping impervious surfaces at per-pixel level is actually a classification task, where impervious and non-impervious surfaces are a combination of various land cover types. Conventional land use/land cover (LULC) includes vegetation, urban area, water, etc., and each land cover type shares similar spectral and spatial characteristics. So, they are often identified individually during the classification procedure. However, impervious/non-impervious surfaces consist of various land cover materials. For instance, impervious surfaces can be made up of dark materials (e.g., asphalt and old concrete) and bright materials (e.g., new concrete and metal), while non-impervious surfaces are also very diverse in materials (e.g., vegetation, water, and base soils). In this study, a two-step approach is employed to estimate the impervious surfaces. Firstly, six land cover types, dark impervious surface (dark IS), bright impervious surface (bright IS), vegetation, water body, bare soil, and shaded areas, are identified with a classification procedure using RF. Secondly, a combination procedure is conducted to combine various land covers into impervious and non-impervious surfaces.

In particular, shaded areas are treated as a single land cover type as they often have unique spectral and spatial characteristics. Moreover, since shaded areas may be impervious (e.g., roads and rooftops) or non-impervious (e.g., greening areas), they are treated as non-impervious surface in the second step of combination in this study. Therefore, dark IS and bright IS are combined as impervious surface, while vegetation, water, bare soil and shade are combined as non-

impervious surface. This may cause some incorrectness since shaded areas may contain impervious surfaces such as roads or rooftops. However, this incorrectness is unavoidable if only optical images are used. This is actually one of the motivations of this study to synergize SAR images to reduce these shaded areas. This assumption will be justified in the Results and discussion section of this paper. Additionally, as misclassification may happen not only between impervious and non-impervious land cover types, but also among different subtypes of impervious or non-impervious types, the accuracy of classification before and after the combination operation may be different. So, in this study, accuracy assessment is conducted on the classification results before and after the combination of impervious/non-impervious surfaces.

Two accuracy indices are employed to assess the accuracy of impervious surface estimation. One is the out-of-bag (OOB) error, which is built in the RF algorithm. The OOB error is calculated based on the training samples, as the training samples are separated into two parts in the RF algorithm, one part for constructing the RF, and the other for evaluating the performance of RF. However, a low OOB does not necessarily guarantee the best performance of a RF when it is applied to other data set other than the training samples. Therefore, the overall accuracy and Kappa coefficient based on the confusion matrix are also employed to assess the accuracy (Jensen, 2007). In addition, reference data are collected through visual interpretation of the optical and SAR images in the three study areas. Higher resolution satellite images from Google Earth near the corresponding dates are used to help the visual interpretation. Moreover, Orthophoto in Hong Kong, with 0.5×0.5 meter resolution, was purchased from the Hong Kong governmental agency, to help improve the quality of visual interpretation of the Hong Kong images. Finally, 1528 samples were collected for Guangzhou area, 1949 samples were collected for Shenzhen area, and 1537 samples were collected for Hong Kong area. Of these reference samples, 50% were used as the training samples to construct the RF, and 50% were used as the test samples to validate the results and test the effectiveness of the method.

4. Results and discussion

4.1. Texture features of optical and SAR images

Four texture measures based on the GLCM were produced from both optical and SAR images of three study areas (Fig. 3). Different characteristics were shown of the features because of not only the optical/SAR sensors but also the resolutions. In the Guangzhou case, urban areas are highlighted in the DISS feature of the optical image, which it is confused with vegetation in other features. In the SAR features, urban areas are more obviously separated, especially in ENT, HOM and ASM features. In the Shenzhen case, vegetation and urban areas are not obviously separated, and shade and water are almost confused in all the features of the optical image. Meanwhile, urban areas are highlighted in the SAR texture features, especially in the areas with high buildings, where the surface roughness brings high backscattering to SAR image. The most unique advantage of SAR features in this case is that shaded areas resulting from high buildings, which are not separable from water in optical features, are separated from water based on SAR features. However, these highlighted areas are only a part of urban areas, and those with lower buildings are not highlighted. So, using only SAR image features is insufficient to extract the impervious surfaces, and combining the two data sources is necessary to extract impervious surfaces more accurately. In the Hong Kong case, the features from optical image do not provide very good separation between urban and non-urban areas. Moreover, water in the northwest part is classified into two cover types due to the diversity of water quality, and thus makes the optical image not suitable for isolating water surfaces in this case. On the other hand, the DISS and ENT features of the SAR images provide good information for distinguishing urban from non-urban areas. Especially, water is well separated in all the features of the SAR images, which provides very good compensation to the optical features.
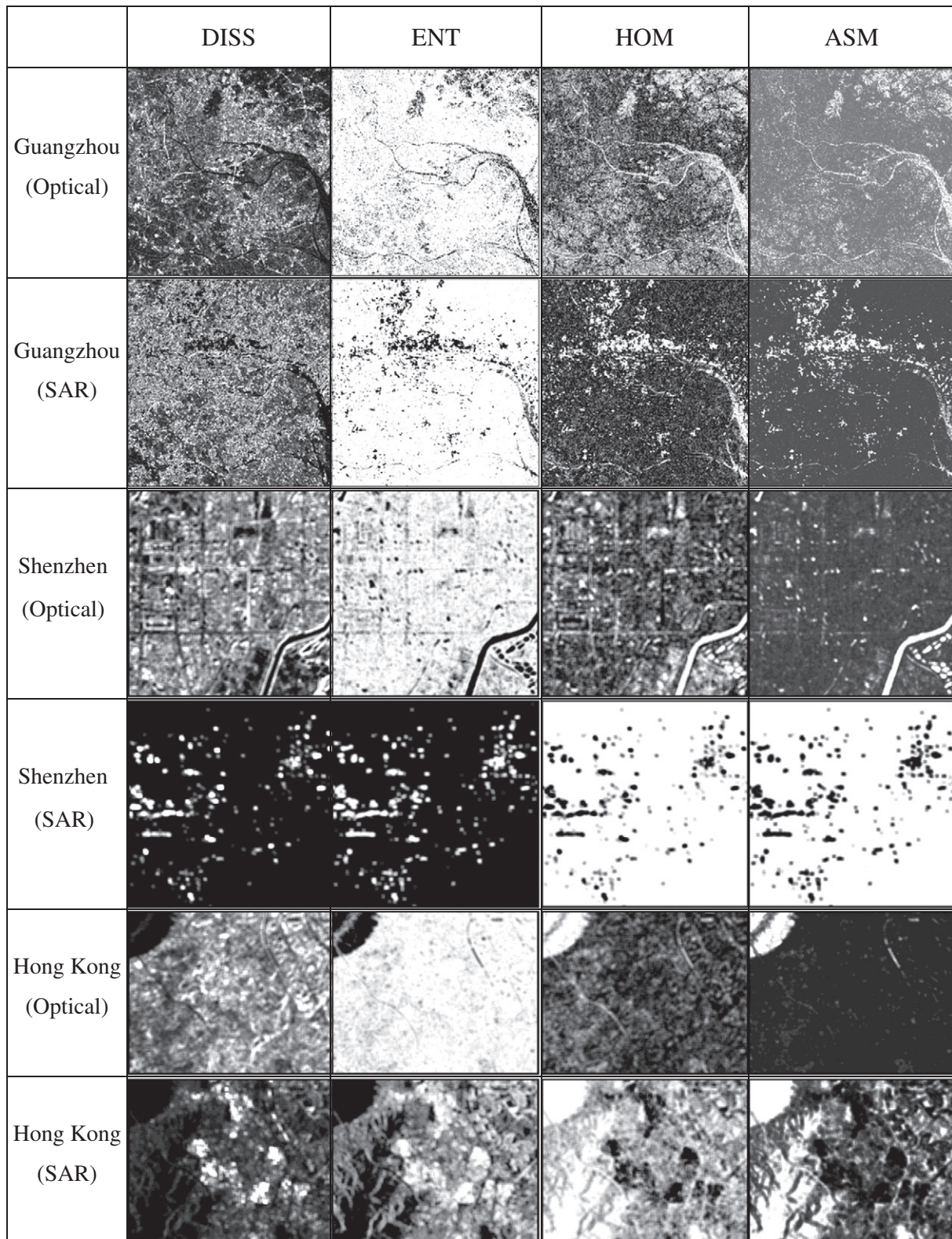
Fig. 3. GLCM texture features of optical and SAR images. DISS: dissimilarity; ENT: entropy; HOM: homogeneity; ASM: the angular second moment.

4.2. Determine the optimal number of features in each decision tree

To test the impacts of the number of variables selected for splitting each node in the decision trees, the number is changed from 1 to the total number of variables. Meanwhile, as the number of decision trees in the RF also influences the results, 4 levels of the number of decision trees are selected to test this influence, that is, 5, 10, 15, and 20, respectively. The Kappa coefficient and the OOB error built in the RF were employed to assess the accuracy of impervious surface estimation. Fig. 4 illustrates the influences of the variation of the number of variables under the selected 4 different numbers of decision trees.
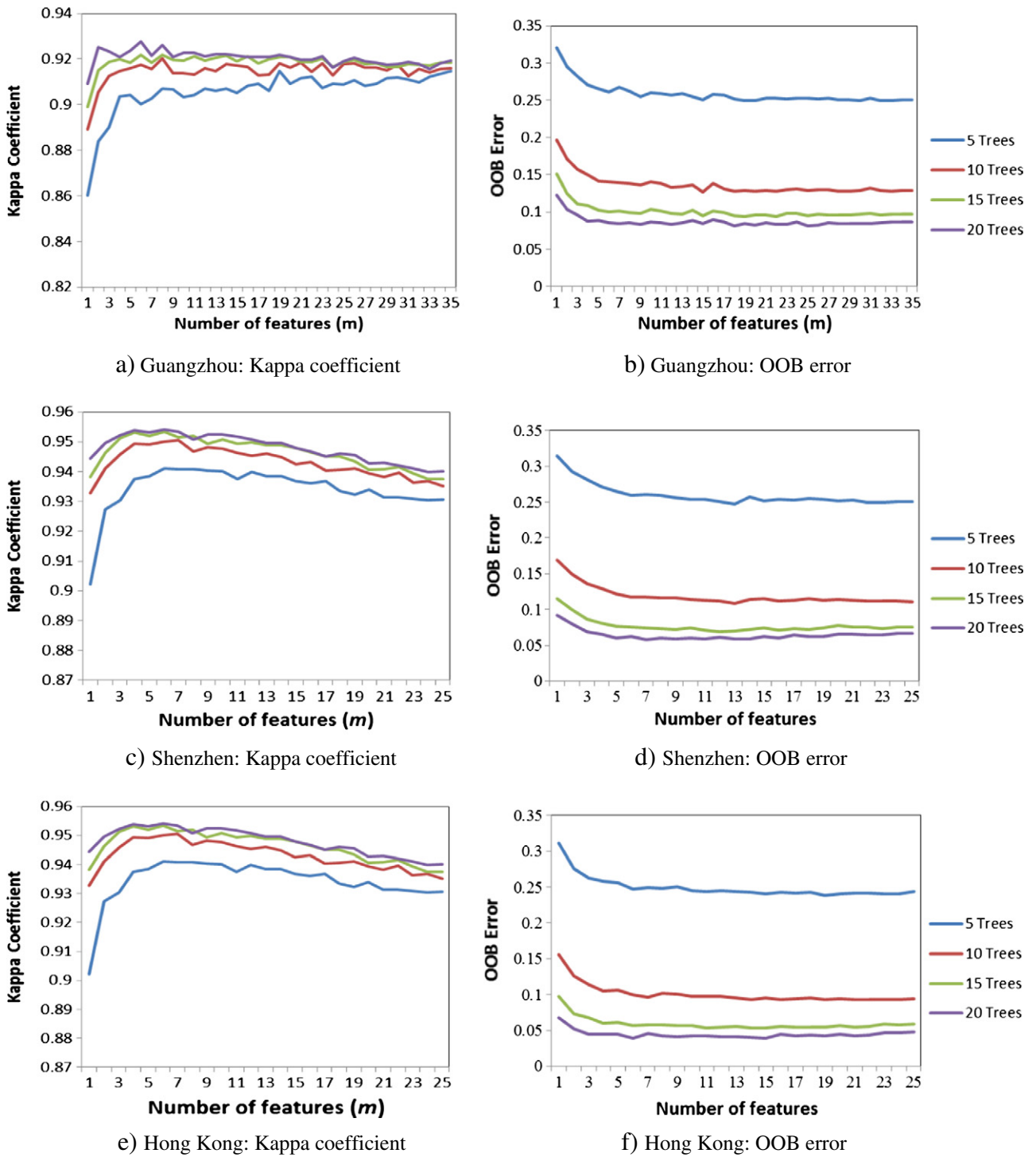
a) Guangzhou: Kappa coefficient

b) Guangzhou: OOB error

c) Shenzhen: Kappa coefficient

d) Shenzhen: OOB error

e) Hong Kong: Kappa coefficient

f) Hong Kong: OOB error

Fig. 4. Impacts of different numbers of variables (or features) in each decision tree.

Firstly, for the Kappa coefficient, a similar pattern is observed for all the 4 different numbers of decision trees. The Kappa coefficient increases quickly at first as the number of selected variables increases, reaches a peak and then decreases steadily with slight fluctuation. The peaks of the curves are located on different positions for the three study areas. They are approximately located on 8 variables, 6 variables, and 6 variables for Guangzhou, Shenzhen, and Hong Kong, respectively. In addition, the different numbers of decision trees can have significant impacts on the Kappa coefficient. The results demonstrate that more decision trees tend to produce a more accurate result, as shown in Fig. 4(a, c, and e). However, the gap between two neighboring curves

becomes smaller and smaller as the number of decision trees increases, and there is a large part of overlay between the two curves for 15 and 20 decision trees for all the three study cases.

Secondly, the OOB error varies with the number of decision trees and study cases, as shown in Fig. 4(b, d, and f). However, the changing pattern of the OOB error is different from that of the Kappa coefficient. At the beginning stage, the OOB error decreases quickly as the number of selected variables increases, and reaches the lowest point. From then on, an increase of the number of variables does not have significant impacts on the OOB error, which becomes relatively steady. Therefore, the curves are almost parallel in the last part though the number of decision

trees differs. For different study cases, the OOB error firstly reaches its lowest point when the number of selected variables is 9, 7 and 6, for Guangzhou, Shenzhen, and Hong Kong, respectively. However, the number of decision trees has significant impacts on the accuracy for a given case even though the pattern of each curve is similar. More decision trees tend to produce a lower OOB curve steady values. However, the gaps between two neighboring curves also become narrower and narrower when the number of decision trees increases.

As reported in previous researches, the number of features in each decision tree was suggested to be the root of the total number of variables from an empirical point of view (Gislason et al., 2006; Stumpf & Kerle, 2011). Thus, according to Gislason et al. (2006) and Stumpf and Kerle (2011), the optimal number of features in each decision tree should be 6, 5, and 5, for Guangzhou, Shenzhen, and Hong Kong, as there are a total of 35, 25, and 25 variables, respectively (Table 2). In this study, the observed optimal number of features is 8, 6, and 6, considering the Kappa coefficient, while this value is 9, 7, and 6, considering the OOB error. This result indicates that the optimal number of variables should be a little bit higher than the root of the total number of variables. In addition, the optimal numbers of variables are not exactly the same by considering the best Kappa coefficient and by considering the lowest OOB error, even though they are closed. This result also indicates that only the built-in accuracy assessment of RF (OOB error) may not reflect the real accuracy of the classification result, as the optimal number of variables differs based on the Kappa coefficient and OOB error. Therefore, additional testing data are needed in order to evaluate the accuracy of the classification using RF. In this study, we set the optimal number of variables according to the best Kappa coefficient, since additional testing samples are more frequently used to validate the classification results in remote sensing applications. Moreover, in order to provide a reference for further similar applications, a simple rule of determining the optimal number of variables in RF is given in Eq. (2), according to the experiment results and discussion.

$$m = \lfloor \sqrt{M} \rfloor + 1 \qquad (2)$$

where m is the optimal number of variables to determine the nodes in a decision tree in RF, and M is the total number of variables. The function $\lfloor x \rfloor$ means the largest integer not greater than x. Eq. (2) indicates that the optimal number of variables is a little bigger than the root of the total number of variables.

4.3. Determine the optimal numbers of decision trees in the Random Forest (RF)

According to the result of Section 4.2, the impacts of the number of decision trees on the classification accuracy can be significant. Even though this impact tends to be reduced when the number of decision trees increases, there are only 4 different numbers of decision trees tested, and further experiments are needed in order to get insight into the impacts of this factor. In this experiment, the number of decision trees is changed to a larger range from 1 to 60. Similarly four different numbers of variables are selected. However, since the total numbers of variables are different for every study cases, 3, 6, 9, and 12 variables are selected for Guangzhou, while 2, 5, 8, and 11 variables are used for Shenzhen and Hong Kong. Corresponding results are illustrated in Fig. 5, where some interesting findings are demonstrated.

Firstly, the Kappa coefficient shows a very tight and similar pattern for the 4 different numbers of variables, that is, it increases quickly as the number of decision trees goes up and then reaches a maximal number. For then on, the Kappa coefficient keeps relatively steady when the number of decision trees continues to increase. What is more interesting is that even though the selected number of variables, the sensors, and the spatial resolutions are different for the three study cases, the starting points where the Kappa coefficient becomes steady are almost

the same, which is approximately 20 decision trees in this research. Nonetheless, the maximal Kappa coefficients are different for the three cases, which are about 0.92 for Guangzhou, 0.95 for Shenzhen, and 0.97 for Hong Kong.

Secondly, the RF built-in accuracy, OOB error, demonstrates a consistent result with the variation of selected number of variables and three study cases. For all the 4 different numbers of variables, the changing pattern of the curves is very similar, and the gap between two curves is highly close. The OOB error firstly drops down very fast and then becomes steady after the number of decision trees reaches 20, which is consistent with the changing pattern of the Kappa coefficient. Additionally, the steady values of the OOB error are different for three study cases. The minimal value of OOB error is approximately 0.09 for Guangzhou, 0.08 for Shenzhen, and 0.05 for Hong Kong.

The experiment results indicate that the optimal number decision trees are independent on the number of selected variables for splitting each node in a decision trees, and it is also independent on the types of sensors and the spatial resolutions of remote sensing images. Since the construction of more decision trees requires more building time of the RF, the optimal number of decision trees should be the first position when the Kappa coefficient reaches the highest and the OOB error reaches its lowest point. In specific application, this optimal number of decision trees can be determined by a statistical procedure similar to this experiment, and for this study, 20 decision trees are the best for a RF to combine the optical and SAR data for impervious surface estimation.

4.4. Impervious surface estimation with optimized RF

In order to perform RF to classify impervious surface using both optical and SAR images, the optimal parameters should be used to configure the RF. According to the results of Section 4.2, the optimal number of variables should be 8, 6, and 6, for Guangzhou, Shenzhen, and Hong Kong, respectively. The optimal number of decision trees should be 20 for all the three cases, according to the results of Section 4.3. Additionally, to evaluate the effectiveness of the combined use of optical and SAR images for impervious surface estimation, optical images alone are used to extract impervious surface for each of the study case. Table 3 shows the total number of variables when using only optical images.

Therefore, according to the empirical rule given in Eq. (2), the optimal number of variables for determining each tree node should be 6, 5, and 5, for Guangzhou, Shenzhen, and Hong Kong. For the number of decision trees, the result in Section 4.3 indicates that 20 decision trees are the best for all the three cases. Since the total number of variables using optical images alone is smaller than that of combining both optical and SAR images, the optimal number of decision trees in this case should probably be smaller than 20. However, Fig. 4 indicates that 20 decision trees would also get the best results when the optimal number is smaller than 20. Therefore, 20 decision trees are also used to build the RF when using optical images alone.

In order to provide a better understanding of the behaviors of the RF algorithm to classify different land cover types, the LULC result before combining the impervious and non-impervious land covers is provided, with the detailed confusion matrices being shown in Table 4. Firstly, for the Guangzhou case, when using only optical image, bright impervious surface (BIS) was easily confused with bare soil (SOI). For instance, 16 pixels of BIS was mistakenly classified as SOI, while 21 pixels of SOI was classified as BIS. So, there are a total of 37 pixels incorrectly classified. However, after combining the optical and SAR images, only 6 pixels of BIS was classified as SOI, and 15 SOI pixels classified as BIS pixels. The total number of misclassified pixels for these two classes was reduced to 21. As a result, with the additional use of SAR image, the overall accuracy (OA) was improved from 91.10% to 93.72%, while the Kappa coefficient increased from 0.8877 to 0.9208. Secondly, for the Shenzhen case, dark impervious surface (DIS) seems to be more easily confused with bare soil (SOI). Before combing optical and SAR data, 4 pixels of SOI was

classified as DIS, and 5 pixels of DIS was classified as SOI. Nevertheless, after combing the two data sources, these two figures were reduced to 0 and 1. Thus, the total number of misclassified pixels between these two classes was reduced from 9 to 1. Moreover, confusion matrices also show that shaded area (SHA) was also confused with DIS, and this situation can also be improved with the additional use of SAR data. In general, the OA increased from 95.89% to 96.41%, and the Kappa coefficient from 0.9507 to 0.9568. Thirdly, for the Hong Kong case, the easy confusion classes turned to SHA and water surface (WAT). While using optical data alone, 10 WAT pixels was classified as SHA, and 4 SHA pixels was classified as WAT. After combining optical and SAR images, only 4 WAT pixels and 3 SHA pixels were incorrectly classified. As a result, the OA increased from 96.88% to 98.44, together with the Kappa coefficient increased from 0.9624 to 0.9812.

In general, two important conclusions can be drawn from the above results. First, when using different combinations of optical and SAR images, the land cover classes that are easily confused are not necessarily the same. This may be caused by the types of sensors, the resolutions
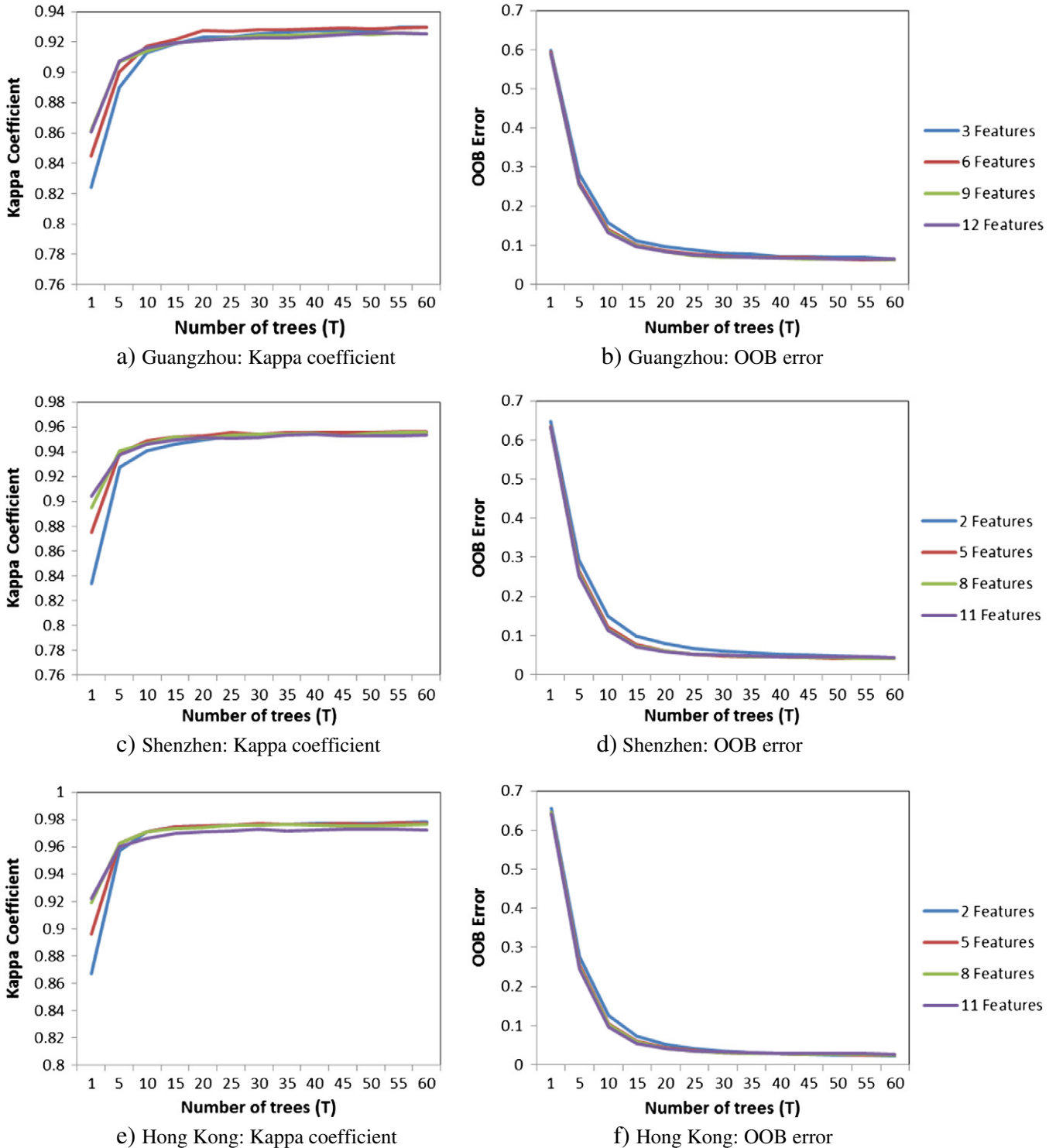

Fig. 5. Impacts of different numbers of trees in the Random Forest.

Table 3
Number of bands and features using optical images alone.

Study area	Number of bands	Number of texture feature images	Total number of images input into RF
Guangzhou	6	24	30
Shenzhen	4	16	20
Hong Kong	4	16	20

of the optical and SAR images, and the study areas. For instance, for higher image resolution of Shenzhen and Hong Kong, shaded areas from tall buildings are more easily detected. These shaded areas would be easily confused with dark impervious surface and water surface. Second, even though the easy confusion classes are not always the same in different study cases, the effectiveness of combing the optical and SAR images can be verified and confirmed with an increase of both overall accuracy and Kappa coefficient.

Then, in the second step, DIS and BIS were combined as impervious surface (IS), while vegetation (VEG), WAT, SOI, and SHA were combined as non-impervious surface (NIS). Fig. 6 demonstrates the impervious surface mapping results with and without the combination of optical and SAR images. Fig. 6 shows a quite consistent IS mapping for the Guangzhou case. Some differences cannot be seen from the mapping results due to the coarse resolution. In the Shenzhen case, a noticeable overestimation can be observed when using optical image alone. This situation was improved significantly after combining both optical and SAR images by reducing the misclassification in the greening areas and shaded areas. In the Hong Kong case, the misclassification of shaded areas and bare soil in the north-eastern part is reduced by incorporating the optical and SAR images. However, negative effect can also be seen in mountainous area in the south-western part due the layover effects of SAR images. The layover effects in mountainous area resulted in high scattering areas which were mistakenly treated as impervious surface. However, this negative effect can be easily removed by using the Digital Elevation Model (DEM) to mask out the mountainous areas.

To better understand the results quantitatively, new confusion matrices are computed in Table 5. The results in Table 5 are generally consistent with that in Table 4, while the OA and Kappa coefficient are generally higher, since the confusion between two impervious classes or two non-impervious classes is removed after the second step of combination. Firstly, Table 5 demonstrates that all the misclassification between IS and NIS was noticeably reduced after combining the optical and SAR images, for Guangzhou, Shenzhen, and Hong Kong. Secondly, the increase of OA ad Kappa coefficient is higher in the Guangzhou case, where OA was improved by 2.5% (=96.73%–94.24%) and Kappa value was increased by 5.48% (=0.9288–0.8740). However, the accuracy increased only about 1% for both OA and Kappa coefficient in the Shenzhen and Hong Kong cases. This result indicates that the combined use of optical and SAR images by RF is more effective for low resolution of images, where there are more confusions between bright impervious surface and bare soil. SAR is sensitive to surface roughness and soil moisture, which is important to differentiate bright impervious surface and bare soil. Therefore, the confusion between these two classes would be greatly reduced, leading to a noticeable increase of the overall accuracy and Kappa coefficient.

Generally, backscattering information in SAR imagery can contribute to improving the accuracy of impervious surface estimation in three different ways. Firstly, since microwave is very sensitive to the geometric configurations of land surface, the backscattering of microwave carries lots of information about geometric features in urban areas, such as the surface roughness determined by buildings and transportation networks. Therefore, SAR images add more distinguishable information between impervious surface and non-impervious surface. Secondly, microwave is also sensitive to moisture including the moisture in bare soil and the water content in vegetation. This characteristic makes SAR imagery easier to separate bare soils and bright impervious surface by reducing the spectral confusion using optical images alone, which is the situation in this study area. Thirdly, SAR remote sensing often works in a side-looking way, leading to a different view angle from that of optical remote sensing. As a result, shaded areas in optical images are often not shaded in the corresponding SAR images, and thus land

Table 4
Confusion matrices for the urban land cover classification.

	Optical						Optical + SAR					
	VEG	DIS	BIS	WAT	SOI	SHA	VEG	DIS	BIS	WAT	SOI	SHA
Guangzhou												
VEG	192	3	0	0	3	0	193	1	0	0	4	0
DIS	1	150	9	1	0	0	0	152	9	0	0	0
BIS	1	9	80	0	16	0	0	7	93	0	6	0
WAT	0	0	0	160	0	0	0	2	0	158	0	0
SOI	3	1	21	0	114	0	3	1	15	0	120	0
SHA	0	0	0	0	0	0	0	0	0	0	0	0
	OA: 91.10% Kappa: 0.8877						OA: 93.72% Kappa: 0.9208					
Shenzhen												
VEG	181	0	0	2	0	0	181	0	0	2	0	0
DIS	0	157	2	0	5	9	0	165	1	0	1	6
BIS	0	1	144	0	1	0	0	0	144	0	2	0
WAT	0	0	0	154	0	1	0	0	0	153	0	2
SOI	1	4	0	0	160	0	1	0	2	0	162	0
SHA	3	11	0	0	0	138	5	13	0	0	0	134
	OA: 95.89% Kappa: 0.9507						OA: 96.41% Kappa: 0.9568					
Hong Kong												
VEG	147	0	0	0	2	0	147	0	0	0	2	0
DIS	0	139	1	0	0	1	0	141	0	0	0	0
BIS	0	0	114	0	0	0	0	0	114	0	0	0
WAT	0	2	0	111	0	10	0	1	0	118	0	4
SOI	1	1	1	0	113	0	0	0	1	0	115	0
SHA	0	1	0	4	0	120	0	1	0	3	0	121
	OA: 96.88% Kappa: 0.9624						OA: 98.44% Kappa: 0.9812					

Note: VEG — vegetation; DIS — dark impervious surface; BIS — bright impervious surface; WAT — water; SOI — soil; SHA — shaded area; OA — overall accuracy.

surface information under the shades in optical images can be seen in SAR images. Therefore, the spectral confusions between shaded areas and dark impervious surface in optical images can be significantly reduced with the additional use of SAR images.

5. Conclusions

Impervious surfaces are attracting increasing attention because they are not only of significance in the urban environment, but also an indicator of urbanization. Nevertheless, accurate mapping of urban impervious surfaces remains challenging due to the spectral diversity of impervious surfaces. This study presents our efforts to synergistically combine the two data sources to improve the mapping of impervious

surfaces by RF algorithm. Three combinations of optical and SAR images, Landsat ETM + and ENVISAT ASAR, SPOT-5 and ENVISAR ASAR, and SPOT-5 and TerraSAR-X, were selected in three study areas, Guangzhou, Shenzhen, and Hong Kong, to test the effectiveness of the methods.

The results indicate some interesting findings about the application of RF to the fusion of optical and SAR data. Firstly, the built-in out-of-bag (OOB) error is insufficient for accuracy assessment, and an assessment with additional reference data is required for combining optical and SAR images using RF. In this study, the overall accuracy (OA) and Kappa coefficient were employed for an additional assessment. The OA and Kappa coefficient show a consistent but slight difference from the OOB error. Secondly, the optimal number of variables (m) for splitting the decision tree nodes in RF should be different from that
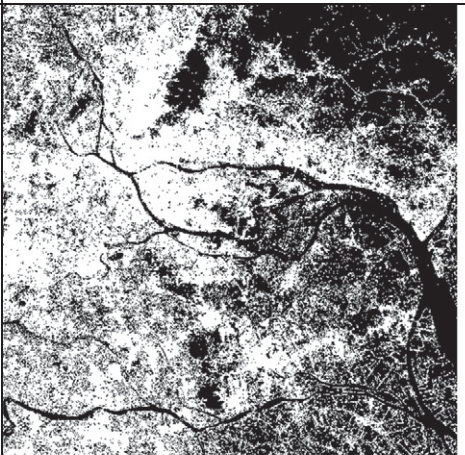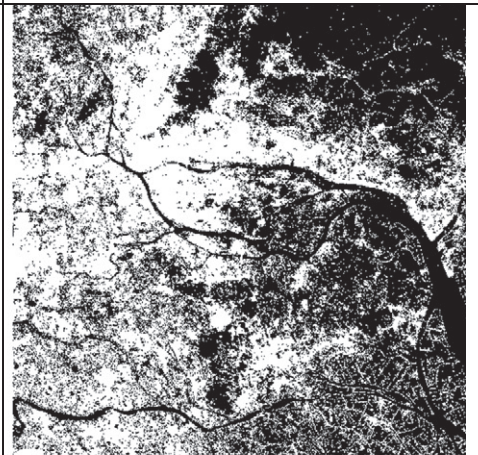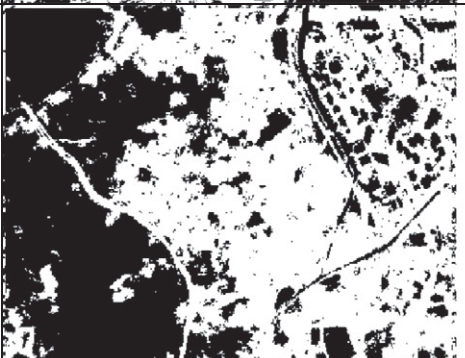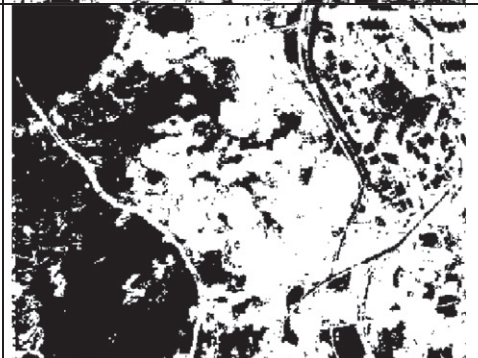

Fig. 6. Results of the impervious surface mapping.

Table 5
Confusion matrices for the impervious surface mapping.

	Optical		Optical + SAR	
	IS	NIS	IS	NIS
Guangzhou				
IS	248	19	261	6
NIS	25	472	19	478
	OA: 94.24%		OA: 96.73%	
	Kappa: 0.8740		Kappa: 0.9288	
Shenzhen				
IS	304	15	310	9
NIS	15	640	15	640
	OA: 96.92%		OA: 97.54%	
	Kappa: 0.9301		Kappa: 0.9443	
Hong Kong				
IS	254	1	255	0
NIS	5	508	3	510
	OA: 99.22%		OA: 99.61%	
	Kappa: 0.9825		Kappa: 0.9912	

Note: IS — impervious surface; NIS — non-impervious surface; OA — overall accuracy.

suggested by the previously reported principle, which indicates *m* as the square root of the total variables. In this study, an empirical relationship (Eq. 2) was provided for determining the parameter *m*. Thirdly, the optimal number of decision trees (*T*) in RF is not sensitive to the resolutions and sensor types of optical and SAR images, and the optimal *T* in this study is 20. Fourthly, the combined use of optical and SAR images by RF is effective to improve the land cover classification and impervious surface estimation, by reducing the confusions between bright impervious surface and bare soil and dark impervious surface and bare soil, as well as shaded area and water surface. Even though the easily-confused land classes tend to be different in different resolutions of images, the effectiveness of combining optical and SAR images is consistent. This improvement is more noticeable for the fusion of optical and SAR images with lower resolutions. The conclusions of this study could serve as an important reference for further applications of optical and SAR images, and as a potential reference for the applications of RF to the fusion of other multi-source remote sensing data.

Acknowledgment

References

Arnold, C. L., & Gibbons, C. J. (1996). Impervious surface coverage — The emergence of a key environmental indicator. *Journal of the American Planning Association, 62*, 243–258.
Breiman, L. (1984). *Classification and regression trees.* Belmont, Calif.: Wadsworth International Group.
Breiman, L. (2001). Random Forests. *Machine Learning, 45*, 5–32.
Calabresi, G. (1996). The use of ERS data for flood monitoring: An overall assessment. *Second ERS application workshop, London, UK* (pp. 237–241).
Cutler, D. R., Edwards, T. C., Beard, K. H., Cutler, A., & Hess, K. T. (2007). Random Forests for classification in ecology. *Ecology, 88*, 2783–2792.
Dell'Acqua, F., & Gamba, P. (2003). Texture-based characterization of urban environments on satellite SAR images. *IEEE Transactions on Geoscience and Remote Sensing, 41*, 153–159.

Deng, C. B., & Wu, C. S. (2012). BCI: A biophysical composition index for remote sensing of urban environments. *Remote Sensing of Environment, 127*, 247–259.
Fan, F. L., Wang, Y. P., & Wang, Z. S. (2008). Temporal and spatial change detecting (1998–2003) and predicting of land use and land cover in Core corridor of Pearl River Delta (China) by using TM and ETM+ images. *Environmental Monitoring and Assessment, 137*, 127–147.
Gislason, P. O., Benediktsson, J. A., & Sveinsson, J. R. (2006). Random Forests for land cover classification. *Pattern Recognition Letters, 27*, 294–300.
Guo, L., Chehata, N., & Boukir, S. (2010). A two-pass Random Forests classification of airborne lidar and image data on urban scenes. *2010 IEEE international conference on image processing* (pp. 1369–1372).
Guo, L., Chehata, N., Mallet, C., & Boukir, S. (2011). Relevance of airborne lidar and multispectral image data for urban scene classification using Random Forests. *ISPRS Journal of Photogrammetry and Remote Sensing, 66*, 56–66.
Hall, D. L., & Llinas, J. (1997). An introduction to multisensor data fusion. *Proceedings of the IEEE, 85*, 6–23.
Ham, J., Chen, Y. C., Crawford, M. M., & Ghosh, J. (2005). Investigation of the Random Forest framework for classification of hyperspectral data. *IEEE Transactions on Geoscience and Remote Sensing, 43*, 492–501.
Haralick, R. M., Shanmuga, K., & Dinstein, I. (1973). Textural features for image classification. *IEEE Transactions on Systems, Man, and Cybernetics, Smc3*, 610–621.
Henderson, F. M., & Xia, Z. G. (1997). SAR applications in human settlement detection, population estimation and urban land use pattern analysis: A status report. *IEEE Transactions on Geoscience and Remote Sensing, 35*, 79–85.
Hurd, J.D., & Civco, D. L. (2004). Temporal characterization of impervious surfaces for the state of Connecticut. *ASPRS Annual Conference Proceedings, Denver, Colorado* (pp. CD-ROM).
Jensen, J. R. (2007). *Introductory digital image processing: A remote sensing perspective* (3rd ed.)London: Pearson Education Ltd.
Jiang, L. M., Liao, M. S., Lin, H., & Yang, L. M. (2009). Synergistic use of optical and InSAR data for urban impervious surface mapping: A case study in Hong Kong. *International Journal of Remote Sensing, 30*, 2781–2796.
Lee, J. S. (1983). Digital image smoothing and the sigma filter. *Computer Vision Graphics and Image Processing, 24*, 255–269.
Leinenkugel, P., Esch, T., & Kuenzer, C. (2011). Settlement detection and impervious surface estimation in the Mekong Delta using optical and SAR remote sensing data. *Remote Sensing of Environment, 115*, 3007–3019.
Lopes, A., Touzi, R., & Nezry, E. (1990). Adaptive speckle filters and scene heterogeneity. *IEEE Transactions on Geoscience and Remote Sensing, 28*, 992–1000.
Lu, D. S., & Weng, Q. H. (2006). Use of impervious surface in urban land-use classification. *Remote Sensing of Environment, 102*, 146–160.
Marceau, D. J., Howarth, P. J., Dubois, J. M. M., & Gratton, D. J. (1990). Evaluation of the gray-level cooccurrence matrix—Method for land-cover classification using spot imagery. *IEEE Transactions on Geoscience and Remote Sensing, 28*, 513–519.
Mingers, J. (1989). An empirical comparison of selection measures for decision-tree induction. *Machine Learning, 3*, 319–342.
Pal, M. (2003). Random Forests for land cover classification. *Igarss 2003: IEEE international geoscience and remote sensing symposium, vols I–Vii, proceedings* (pp. 3510–3512).
Puissant, A., Hirsch, J., & Weber, C. (2005). The utility of texture analysis to improve per-pixel classification for high to very high spatial resolution imagery. *International Journal of Remote Sensing, 26*, 733–745.
Quinlan, J. R. (1986). Induction of decision trees. *Machine Learning, 1*, 81–106.
Rokach, L. (2010). Ensemble-based classifiers. *Artificial Intelligence Review, 33*, 1–39.
Soergel, U. (2010). *Radar remote sensing of urban areas.* Heidelberg: Springer, 133–159.
Stasolla, M., & Gamba, P. (2008). Spatial indexes for the extraction of formal and informal human settlements from high-resolution SAR images. *IEEE Journal of Selected Topics in Applied Earth Observations and Remote Sensing, 1*, 98–106.
Stumpf, A., & Kerle, N. (2011). Object-oriented mapping of landslides using Random Forests. *Remote Sensing of Environment, 115*, 2564–2577.
Sun, Z. C., Guo, H. D., Li, X. W., Lu, L. L., & Du, X. P. (2011). Estimating urban impervious surfaces from Landsat-5 TM imagery using multilayer perceptron neural network and support vector machine. *Journal of Applied Remote Sensing, 5*.
Tison, C., Nicolas, J. M., Tupin, F., & Maitre, H. (2004). A new statistical model for Markovian classification of urban areas in high-resolution SAR images. *IEEE Transactions on Geoscience and Remote Sensing, 42*, 2046–2057.
Waske, B., & van der Linden, S. (2008). Classifying multilevel imagery from SAR and optical sensors by decision fusion. *IEEE Transactions on Geoscience and Remote Sensing, 46*, 1457–1466.
Weng, Q. H. (2001). Modeling urban growth effects on surface runoff with the integration of remote sensing and GIS. *Environmental Management, 28*, 737–748.
Weng, Q. H. (2012). Remote sensing of impervious surfaces in the urban areas: Requirements, methods, and trends. *Remote Sensing of Environment, 117*, 34–49.
Weng, Q. H., & Hu, X. F. (2008). Medium spatial resolution satellite imagery for estimating and mapping urban impervious surfaces using LSMA and ANN. *IEEE Transactions on Geoscience and Remote Sensing, 46*, 2397–2406.
Weng, Q. H., Lu, D. S., & Liang, B. Q. (2006). Urban surface biophysical descriptors and land surface temperature variations. *Photogrammetric Engineering and Remote Sensing, 72*, 1275–1286.
Wu, C. S. (2004). Normalized spectral mixture analysis for monitoring urban composition using ETM plus imagery. *Remote Sensing of Environment, 93*, 480–492.
Wu, C. S., & Murray, A. T. (2003). Estimating impervious surface distribution by spectral mixture analysis. *Remote Sensing of Environment, 84*, 493–505.
Xie, H., Pierce, L. E., & Ulaby, F. T. (2002). SAR speckle reduction using wavelet denoising and Markov random field modeling. *IEEE Transactions on Geoscience and Remote Sensing, 40*, 2196–2212.

Yang, L. M., Jiang, L. M., Lin, H., & Liao, M. S. (2009). Quantifying sub-pixel urban impervi-
ous surface through fusion of optical and InSAR imagery. *Giscience & Remote Sensing,*
46, 161–171.

Yang, L. M., Xian, G., Klaver, J. M., & Deal, B. (2003). Urban land-cover change detection
through sub-pixel imperviousness mapping using remotely sensed data.
Photogrammetric Engineering and Remote Sensing, 69, 1003–1010.

Yu, X. W., Hyyppa, J., Vastaranta, M., Holopainen, M., & Viitala, R. (2011). Predicting
individual tree attributes from airborne laser point clouds based on the Random
Forests technique. *ISPRS Journal of Photogrammetry and Remote Sensing, 66,* 28–37.

Yuan, F., & Bauer, M. E. (2007). Comparison of impervious surface area and normalized
difference vegetation index as indicators of surface urban heat island effects in
Landsat imagery. *Remote Sensing of Environment, 106,* 375–386.

Zambon, M., Lawrence, R., Bunn, A., & Powell, S. (2006). Effect of alternative splitting rules
on image processing using classification tree analysis. *Photogrammetric Engineering*
and Remote Sensing, 72, 25–30.

Zhang, H., Zhang, Y., & Lin, H. (2012). A comparison study of impervious surfaces estima-
tion using optical and SAR remote sensing images. *International Journal of Applied*
Earth Observation and Geoinformation, 18, 148–156.

Zhang, J. X., Yang, J. H., Zhao, Z., Li, H. T., & Zhang, Y. H. (2010). Block-regression based
fusion of optical and SAR imagery for feature enhancement. *International Journal of*
Remote Sensing, 31, 2325–2345.

Zhang, Y. H., Hu, M., Zhong, L. J., Wiedensohler, A., Liu, S.C., Andreae, M.O., et al. (2008).
Regional integrated experiments on air quality over Pearl River Delta 2004
(PRIDE-PRD2004): Overview. *Atmospheric Environment, 42,* 6157–6173.